

## Research Article

# Structural and Compositional Characterization of Fungus-Derived Pyrolytic Carbon Architectures

Brennan Campbell,<sup>1</sup> Robert Ionescu,<sup>1</sup> Cengiz S. Ozkan,<sup>2</sup> and Mihrimah Ozkan<sup>3</sup>

<sup>1</sup>Materials Science and Engineering Program, University of California, Riverside, CA 92521, USA

<sup>2</sup>Materials Science and Engineering Program, Department of Mechanical Engineering, University of California, Riverside, CA 92521, USA

<sup>3</sup>Materials Science and Engineering Program, Department of Electrical Engineering and Department of Chemistry, University of California, Riverside, CA 92521, USA

Correspondence should be addressed to Cengiz S. Ozkan; [cozkan@engr.ucr.edu](mailto:cozkan@engr.ucr.edu) and Mihrimah Ozkan; [mihri@ee.ucr.edu](mailto:mihri@ee.ucr.edu)

Received 30 January 2016; Revised 5 June 2016; Accepted 14 June 2016

Academic Editor: Akhila K. Sahu

Copyright © 2016 Brennan Campbell et al. This is an open access article distributed under the Creative Commons Attribution License, which permits unrestricted use, distribution, and reproduction in any medium, provided the original work is properly cited.

Three distinctive pyrolytic carbon structures, derived from three specific tissues of *Agaricus bisporus* mushroom, were studied and characterized. The three structures discovered within the stalk, cap, and cap skin tissues were found to contain unique microarchitectures, which were preserved upon anoxic carbonization. Experiments also revealed the formation of salt pockets and deposits within each microarchitecture, leading to a potential natural hard-template method for porous carbon structures.

## 1. Introduction

Functional carbonaceous materials are becoming increasingly attractive because of their light weight, low cost, versatility, mechanical properties, and electronic conductivity [1, 2]. Carbons of varying micro- and nanostructures are potentially useful in a multitude of applications, from bulk and nanoscale materials to structural and energy storage materials. The sources of carbon chosen for engineering purposes depend on the processing techniques necessary to produce such carbon, its scalability, and the specific properties desired. For example, carbon nanotubes (CNTs) have been the center of much interest to scientists and engineers for their wide body of applications [3, 4]. Guo et al. used CVD-grown CNTs to confine sulfur in Li-S batteries with excellent efficiency and capacity over many charge-discharge cycles [5]. Amorphous carbons are also being studied for their diverse applications and their ability to form pores of various sizes, acquiring microporosity (<2 nm pores), mesoporosity (2 < x < 50 nm pores), or macroporosity (>50 nm pores). Ouyang et al., for instance, have recently made progress in achieving amorphous, microporous carbon spheres with high polydispersity through polystyrene hypercrosslinking and hydrothermal

decomposition [6]. The resultant nanospheres have great potential use in batteries, catalysis, medicine, and so forth [7, 8]. Nowadays, carbonaceous foams are also of increasing interest, due to their freestanding nature, interconnectedness, and applications as bulk materials. Depardieu et al. recently developed a carbonaceous foam as a lithium-sulfur battery electrode, with macroporosity as well as mesoporosity. Using both a silica hard template and triblock copolymer soft templates, a phenolic resin was introduced and pyrolyzed to form the porous carbon monolith [9]. Similar carbon foam-like structures have been obtained through the carbonization of biomass in the absence of oxygen. This method of biomediation yields diverse micro- and nanostructured carbon materials, which can often be used as a freestanding monolith or milled to form powders, depending on the application. A biomass-derived carbon foam was developed by Wang et al. by liquefying birch sawdust into its resinous constituents, until it was able to become foamed and carbonized [10]. While high surface area and bulk density were accomplished, the process required numerous steps, several toxic solvents, and strong acids and bases, ultimately making it an economically and environmentally costly material to scale up.

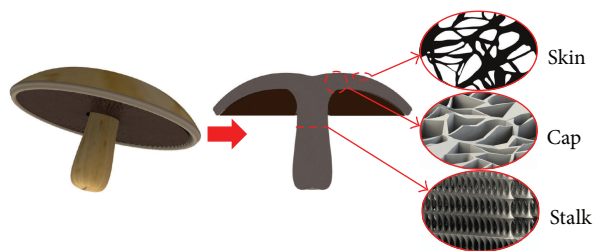


FIGURE 1: Schematic representation of the PM specimen, the sectioning process, and the modelled architecture of CST, CT, and ST, respectively.

For the first time, we report on the pyrolysis-induced microarchitectures of three specific tissues of *Agaricus bisporus*, commonly known as the Portobello mushroom (PM). The elemental compositions and structural characteristics of Portobello sections were analyzed using various microscopic and spectroscopic techniques. The sections under study were the cap, stalk, and cap skin, each having distinct postcarbonization microarchitectures, which have profound potential to serve as functional and structural carbonaceous materials across various industries. Recently, we have demonstrated one of these pristine, freestanding carbon architectures as a high-performance carbon anode for lithium-ion batteries [11]. The resulting structures are obtained facilely, through a low-cost and scalable heat-treatment process that requires no expensive solvents, precursors, or work-ups. In this work, freestanding carbonaceous materials were synthesized via heat treatment of various tissues of the fungal fruiting body of *A. bisporus*. As summarized in Figure 1, PMs were obtained, tissue samples were sectioned using razor blades and hole punches, and the samples were pyrolyzed. The carbonized PM tissues under study were cap tissue (CT), stalk tissue (ST), and cap skin tissue (CST). Initial SEM imaging of the carbonized PM tissue morphologies confirmed that the microstructures of the resulting carbonaceous materials were distinct from one another. What is more, the 3D configurations of each respective microstructure seem to have compelling functional patterns, which could be correlated to the biological utility of a living PM. While the CT displayed a random, cavernous foam-like microarchitecture, the ST exhibits a unidirectional sinter column-like arrangement, and the CST forms thin, high aspect ratio, interconnected carbon nanoribbons.

## 2. Materials and Methods

A typical experiment was carried out as follows: organic PMs were purchased from local markets and cleaned with DI H<sub>2</sub>O. The stalks were removed from the caps, the skins were peeled from the caps, and the gills (located under the “hood” formed by the cap) were scraped out. Next, razor blades were used to slice the cap tissue into thin slices (~5 mm), as was the stalk tissue. The stalk tissue was sliced both vertically and horizontally to observe the anisotropic architecture. All samples were placed in a vacuum oven at 80°C for 24 hours to remove as much moisture as possible.

All samples were then transferred to a tube furnace. Under 700 Torr, argon gas was flowed at 300 SCCM, and the temperature was ramped from 21 to 600°C over 60 minutes. The temperature was held at 600°C for 5 hours and then allowed to cool slowly. The CTs, STs, and CSTs were removed and analyzed. A number of the samples were studied as-synthesized, while others were washed in DI H<sub>2</sub>O to further understand their composition. Additional experiments were carried out at higher temperatures, during which the escaping of molten KCl salts induced the formation of pores of various sizes, a phenomenon which was first reported in our previous lithium-ion battery work [11].

## 3. Results and Discussion

Morphologies of the carbonized CTs, STs, and CSTs were studied using scanning electron microscopy (SEM). Figures 2(a)–2(c) capture the microarchitecture of the CTs, which is a disordered carbon foam-like structure. The walls of the foam range between a few microns and several tens of microns. In general, the structure of the CT is very macroporous and random. The structure is also decorated with small, round pockets, which were found from later study to be biological salts (principally KCl) localized into pockets and surface deposits. A vertical ST section is shown in Figures 2(d)–2(f), revealing a carbon microarchitecture resembling stacked, vertically aligned, and unidirectional sinter columns. At low magnification (Figure 2(d)), the uniform, aligned ordering of the sinter columns is evident. The linear direction from the lower-left-hand corner of the image to the upper-right-hand corner is parallel to the line formed from the base of the PM stalk to the center of the cap. It is thus inferred that, in the live PM specimen, this arrangement contributes to the strength of the stalk and the ability of the stalk structure to support the large cap. The cap of a mature PM can make up anywhere between 70 and 80% of the weight of the entire fruiting body, according to our gravimetric measurements. Typically, the diameter of the middle of the sinter columns is anywhere between 5 and 10 μm, while the bases of the columns and connection points are several tens of microns thick. There is also evidence that the ordered columns are hierarchical in nature; optical microscopy of the stalk tissue before carbonization, shown in Figures S1(c)–S1(d) in Supplementary Material available online at <http://dx.doi.org/10.1155/2016/9843875>, seems to indicate that larger columns are comprised of smaller fibers, which may contribute to the size variation of columns seen under SEM. Similar to the CTs, the STs appear to contain salt pockets, seen clearly in Figure 2(e). Finally, the CST micrographs display an interconnected carbon nanoribbon architecture, observed in Figures 2(g)–2(i). This structure is distinct from the CT and ST in that these ribbons are remarkably thin; they are approximately 23 nm in thickness, more clearly seen in Figure S2. The low thickness of the ribbons partially renders them transparent under SEM. The width of the nanoribbons varies from 5–6 μm to tens of microns. The CST samples also exhibit salt and pockets and deposits which predominantly form diameters on the order

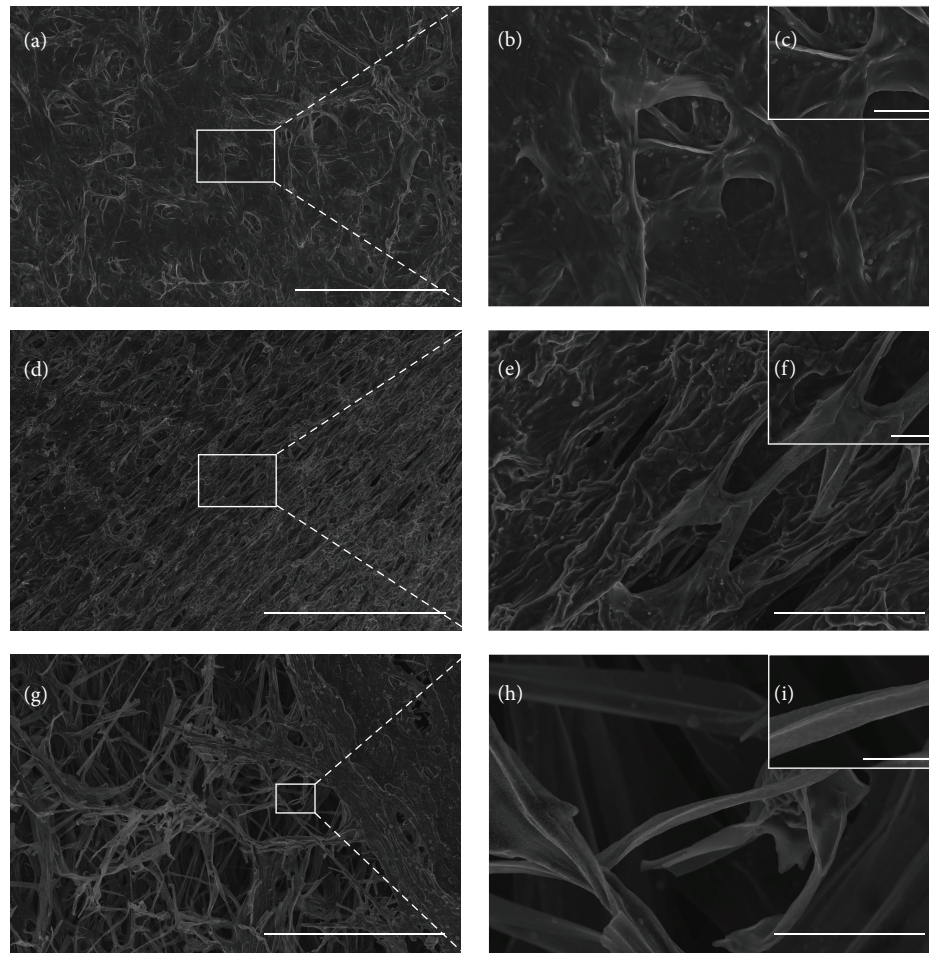


FIGURE 2: SEM micrographs, low to high magnification, of CT (a–c) (scale bars = 200  $\mu\text{m}$ , 40  $\mu\text{m}$ , and 10  $\mu\text{m}$ ), ST (d–f) (scale bars = 400  $\mu\text{m}$ , 50  $\mu\text{m}$ , and 10  $\mu\text{m}$ ), and CST (g–i) (scale bars = 300  $\mu\text{m}$ , 20  $\mu\text{m}$ , and 4  $\mu\text{m}$ ).

of nanometers to multiple microns (see Figures 2(i) and S3). The generally high aspect ratio of the CST nanoribbons leads to the hypothesis that they, depending on the processing temperature, would exhibit good performance in devices which require high surface area, such as electric double-layer capacitors, which depend on the ability to store surface charge [12].

In addition to observing morphology, compositional analysis was conducted on the PM samples. Using high-resolution energy-dispersive X-ray spectroscopy (EDS), great detail was achieved in terms of the elemental distribution in the CT, ST, and CST; elemental mapping of the pristine and unwashed CT, as well as the CT after washing in DI H<sub>2</sub>O overnight, is shown in Figures 3 and 4, respectively. The elemental maps of the ST and CST, before and after DI H<sub>2</sub>O washing, are included in Figures S4 and S5, respectively. A defining attribute of this analysis is the presence of biological salts that are present before the DI H<sub>2</sub>O washing (Figures 3(a) and 3(b)) and are dramatically reduced after the washing (Figures 4(a) and 4(b)). Interestingly, the salts become located in pockets of various sizes, which are well highlighted in the element composite image in Figure 3(b). These disappear

in the postwash composite image in Figure 4(b). While the weight percentage of oxygen is marginally changed from DI H<sub>2</sub>O washing, carbon is significantly increased, and nearly every other major mineral present is decreased. Notably, the K and Cl peaks are diminished from 16 and 3.3 wt.%, respectively (Figure 3(d)), to 5.1 and virtually 0 wt.%, respectively (Figure 4(d)). Thus, the primary elements found in the salts of the PM are K and P, which is consistent with literature values for fresh *Agaricus* species [13, 14]. The P content remains relatively constant after DI H<sub>2</sub>O washing; this somewhat correlates with the unchanged O concentration and may be attributed to the presence of phosphate species and phospholipids, which typically occur in *A. bisporus* [15, 16]. The phenomenon of salt-pocketing upon carbonization in this particular fungal biomass has important implications when it comes to carbon microarchitecture engineering; depending on heat-treatment temperature, these pockets may serve as a natural hard template for generating pores [11]. Furthermore, this phenomenon should compel further comparative study into the roles of biological salts in carbonization of other various forms of biomass such as plant matter, due to the differences in organic polymer/oligomer

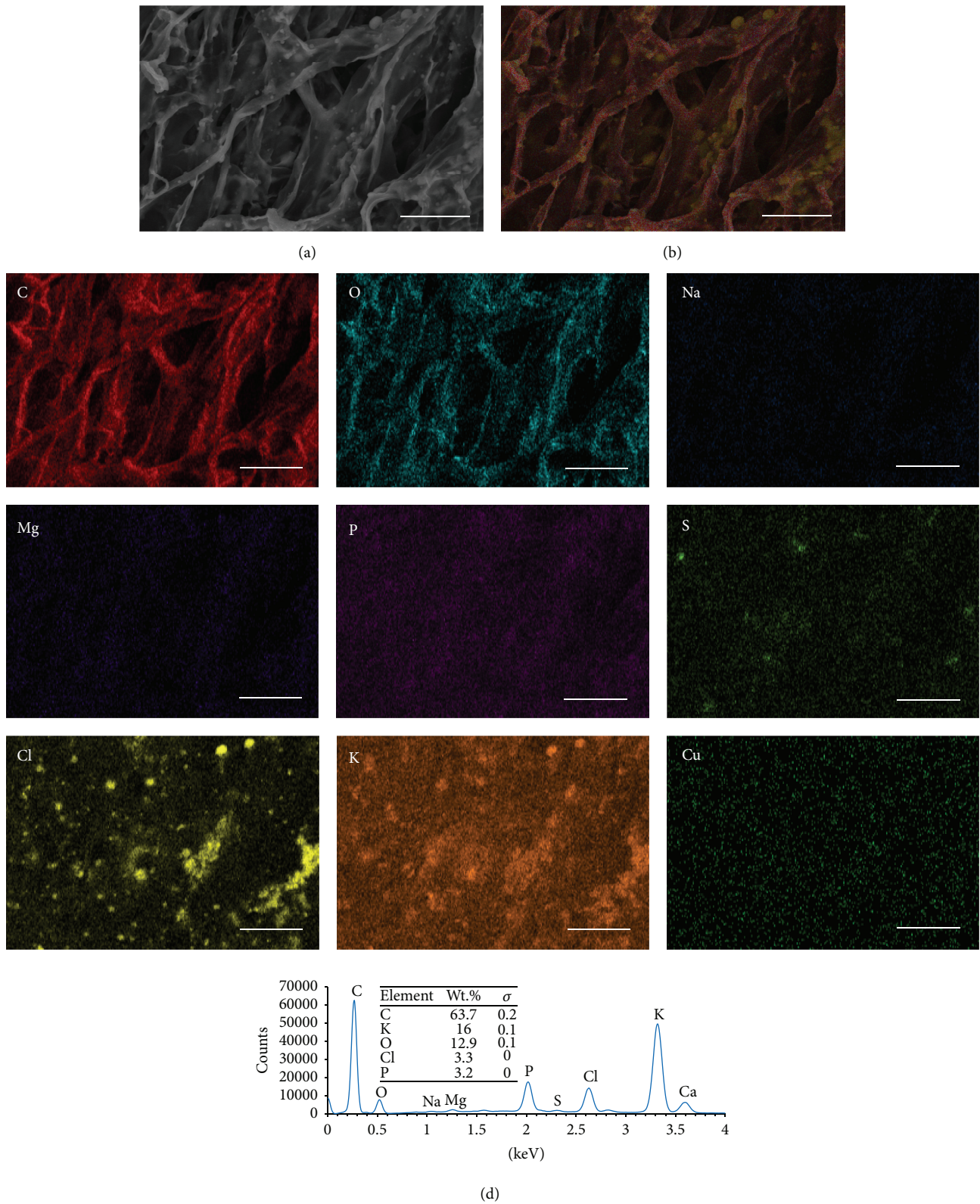


FIGURE 3: Elemental mapping of CT before DI H<sub>2</sub>O wash, including the raw electron image (a), composite image (b), and maps of most prominent elements in the specimen (all scale bars = 25  $\mu$ m), with accompanying EDS spectrum (d).

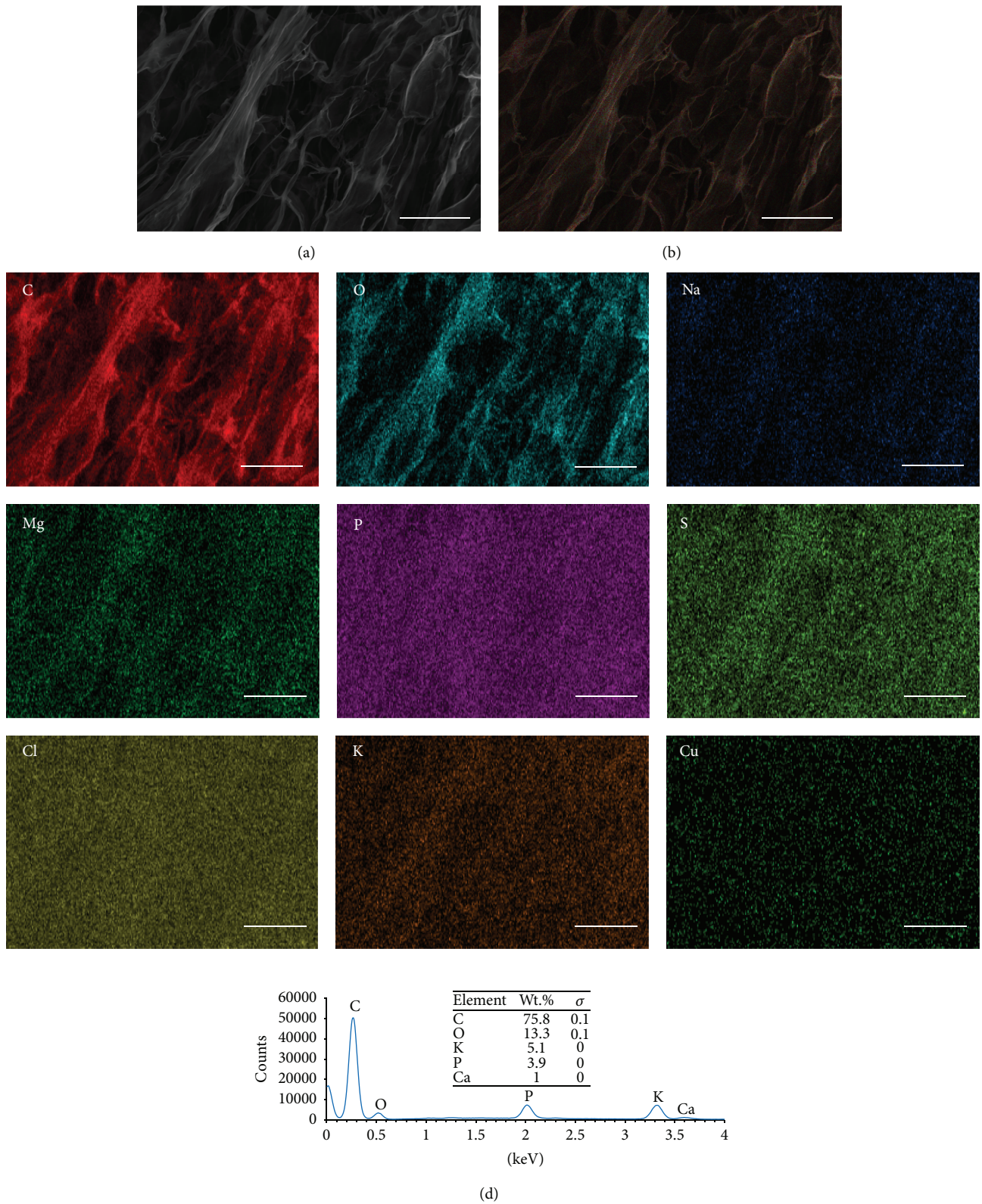


FIGURE 4: Elemental mapping of CT after DI H<sub>2</sub>O wash, including the raw electron image (a), composite image (b), and maps of most prominent elements in the specimen (all scale bars = 25  $\mu$ m), with accompanying EDS spectrum (d).

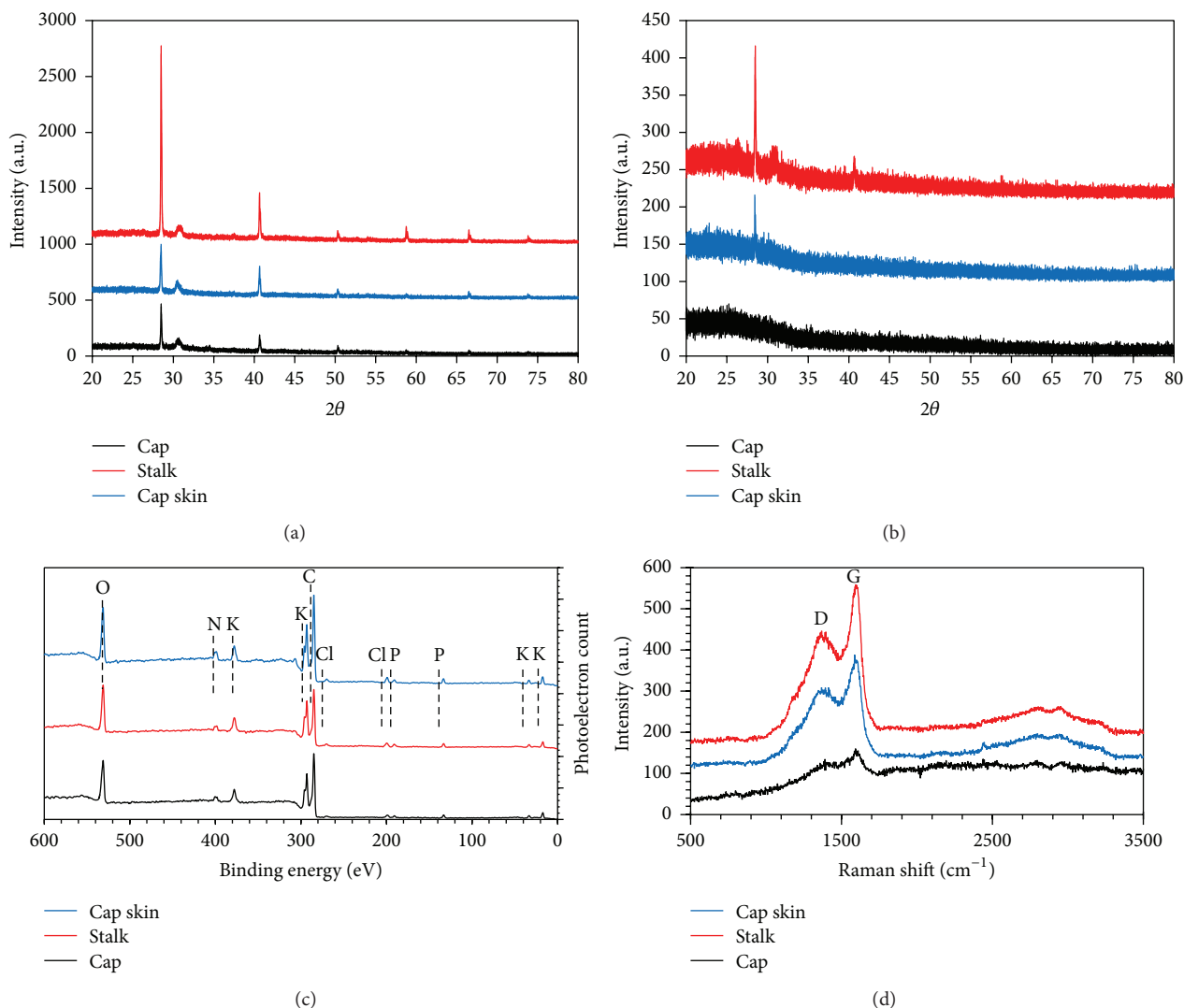


FIGURE 5: Spectral data from CT (cap), ST (stalk), and CST (cap skin), including XRD spectra from pre-DI H<sub>2</sub>O wash (a), post-DI H<sub>2</sub>O wash (b), XPS of pristine, unwashed samples (c), and Raman spectra of washed CT, ST, and CST samples (d).

compositions. The organics in the cell walls of *A. bisporus*, unlike plants, contain a relatively high concentration of the polysaccharide chitin, upwards of about 10% dry mass, with the stalk tissues containing slightly higher concentrations [17]. Chitin is as an important, nitrogen-containing structural polysaccharide for vertical growth of the fungal fruiting body and is vital for the fungus survival through spore dispersal. Scanning electron microscopy and energy-dispersive X-ray spectroscopy characterization were performed using an FEI Nova NanoSEM 450.

Spectral data were obtained for the three carbonized tissues, including X-ray diffraction (XRD) and X-ray photoelectron spectroscopy (XPS), to analyze phases present in the as-prepared carbonized samples. Pristine samples of the CT, ST, and CST were prepared by carbonizing slices of each tissue with a thickness of 3-4 mm, which resulted in carbonized disk-shaped samples of about 1-3 mm in thickness. The strong peaks observed in Figure 5(a) at  $2\theta$ : 28.5, 40.6, 51.0,

58.8, 66.5, and 74.0 correlate to the diffraction angles of cubic crystalline KCl [18]. The less intense, rounder peak at  $2\theta$ : 31.3, however, is characteristic of the primary peak of NaCl [19]. The XRD spectra for the pristine, unwashed samples indicate principally alkali metal halide salts. Finally, the slightly elevated downfield region (between  $2\theta$ : 20 and 35) correlates to amorphous carbon [20]. The XRD spectrum of post-DI H<sub>2</sub>O washed samples is shown in Figure 5(b), where it is shown that the halide salt presence is significantly reduced. There is still a noticeable presence of KCl and NaCl in the samples, although the intensity diminished by a large factor, which agrees well with the postwash EDS of the CT. The elevated downfield region associated with amorphous carbon is also more prominent in the postwash XRD analysis. Overall, the order of strongest halide salt peaks from largest to smallest is the ST, CST, and CT, respectively. For the postwash XRD CT sample, the salt peaks are almost entirely absent. XPS was also used to identify surface composition and

bonding in the carbon architectures. The PM samples used for XPS were pristine, unwashed, and in their freestanding form to more accurately identify species other than typical organic bonds. For each sample type, the signature peaks for C, O, K, P, Cl, and N were prominent. The strength of each peak showed no significant change between tissue types. The strong presence of K observed in all forms of analysis in this study is expected and is not attributed to contamination of the specimen before purchasing. Raman spectroscopy was carried out on the three freestanding mushroom tissues to analyze the type of carbon under study. After the annealing between 500 and 600°C, Raman spectra were taken and the data is shown in Figure 5(d). The Raman data above gives good insight into the crystalline nature of the fungus-derived carbons. It has been determined that the D and G peaks,  $\sim 1365$  and  $1594\text{ cm}^{-1}$ , respectively, indicated the presence of graphitic carbon. Upfield, between  $2500$  and  $3300\text{ cm}^{-1}$ , there is a large broad hump with a noticeable pair of peaks at  $2804$  and  $2951\text{ cm}^{-1}$ , respectively. The exact nature of the pyrolytic carbon is a mixture of allotropes but mostly resembles hard carbon type, with strong graphitic nature. The graphite microdomains, however, are turbostratically arranged, meaning that there is short-range order as well as significant 3D rotation of the microdomains. It can be seen from this data, based on the peak intensities, that the CT has the lowest crystallinity and the ST has the highest crystallinity, with the CST lying in between.

#### 4. Conclusions

The examination of Portobello mushroom (PM) sections from the cap tissue (CT), stalk tissue (ST), and cap skin tissue (CST) was carried out after carbonization at 600°C for 5 hours. The resulting architectures at the microscale lead to new insights which are compelling for future biomimetic and/or bioinspired materials engineering endeavours. The carbonization of the chitin-containing PM biomass resulted in microstructures of the following types: CT forms a randomly oriented, macroporous, thicker-walled carbon foam structure; ST forms a unidirectional, elongated sinter column-like structure; and CST assumes an interconnected carbon nanoribbon structure. The elemental compositions of each section were analyzed through EDS, XRD, and XPS. Results indicate that the as-synthesized samples have, in addition to carbon and oxygen, a significantly high concentration of potassium, phosphorus, and chlorides, among other trace minerals, located in pockets and surface deposits. Raman analysis suggests that the carbon is a graphitic, yet highly disordered, carbon most closely resembling hard carbons.

#### Competing Interests

The authors declare that there is no conflict of interests regarding the publication of this paper.

#### Acknowledgments

Financial support from the UC Riverside is gratefully acknowledged. XPS measurements were recorded at UC

Riverside with support from the National Science Foundation under Grant no. DMR-0958796. The authors also would like to thank Mr. Lauro Zavala for artistic contributions.

#### References

- [1] H. Chen, M. B. Müller, K. J. Gilmore, G. G. Wallace, and D. Li, "Mechanically strong, electrically conductive, and biocompatible graphene paper," *Advanced Materials*, vol. 20, no. 18, pp. 3557–3561, 2008.
- [2] A. Lu, G. Hao, Q. Sun, X. Zhang, and W. Li, "Chemical synthesis of carbon materials with intriguing nanostructure and morphology," *Macromolecular Chemistry and Physics*, vol. 213, no. 10–11, pp. 1107–1131, 2012.
- [3] C. Gao, Z. Guo, J.-H. Liu, and X.-J. Huang, "The new age of carbon nanotubes: an updated review of functionalized carbon nanotubes in electrochemical sensors," *Nanoscale*, vol. 4, no. 6, pp. 1948–1963, 2012.
- [4] M. F. L. De Volder, S. H. Tawfik, R. H. Baughman, and A. J. Hart, "Carbon nanotubes: present and future commercial applications," *Science*, vol. 339, no. 6119, pp. 535–539, 2013.
- [5] J. Guo, Y. Xu, and C. Wang, "Sulfur-impregnated disordered carbon nanotubes cathode for lithium-sulfur batteries," *Nano Letters*, vol. 11, no. 10, pp. 4288–4294, 2011.
- [6] Y. Ouyang, H. Shi, R. Fu, and D. Wu, "Highly monodisperse microporous polymeric and carbonaceous nanospheres with multifunctional properties," *Scientific Reports*, vol. 3, article 1430, 2013.
- [7] B. Zhang, X. Qin, G. R. Li, and X. P. Gao, "Enhancement of long stability of sulfur cathode by encapsulating sulfur into micropores of carbon spheres," *Energy & Environmental Science*, vol. 3, no. 10, pp. 1531–1537, 2010.
- [8] W.-K. Oh, H. Yoon, and J. Jang, "Size control of magnetic carbon nanoparticles for drug delivery," *Biomaterials*, vol. 31, no. 6, pp. 1342–1348, 2010.
- [9] M. Depardieu, R. Janot, C. Sanchez et al., "Carbonaceous multiscale-cellular foams as novel electrodes for stable, efficient lithium-sulfur batteries," *RSC Advances*, vol. 4, no. 46, pp. 23971–23976, 2014.
- [10] R. Wang, W. Li, and S. Liu, "A porous carbon foam prepared from liquefied birch sawdust," *Journal of Materials Science*, vol. 47, no. 4, pp. 1977–1984, 2012.
- [11] B. Campbell, R. Ionescu, Z. Favors, C. S. Ozkan, and M. Ozkan, "Bio-derived, binderless, hierarchically porous carbon anodes for Li-ion batteries," *Scientific Reports*, vol. 5, Article ID 14575, 2015.
- [12] C. Zhang, Z. Peng, J. Lin et al., "Splitting of a vertical multiwalled carbon nanotube carpet to a graphene nanoribbon carpet and its use in supercapacitors," *ACS Nano*, vol. 7, no. 6, pp. 5151–5159, 2013.
- [13] J. Vetter, "Chemical composition of fresh and conserved *Agaricus bisporus* mushroom," *European Food Research and Technology*, vol. 217, no. 1, pp. 10–12, 2003.
- [14] P. Mattila, K. Könkö, M. Euroola et al., "Contents of vitamins, mineral elements, and some phenolic compounds in cultivated mushrooms," *Journal of Agricultural and Food Chemistry*, vol. 49, no. 5, pp. 2343–2348, 2001.
- [15] A. Braaksma, P. van der Meer, and D. J. Schaap, "Polyphosphate accumulation in the senescing mushroom *Agaricus bisporus*," *Postharvest Biology and Technology*, vol. 8, no. 2, pp. 121–127, 1996.

- [16] P. F. S. Byrne and P. J. Brennan, "The lipids of *Agaricus bisporus*," *Microbiology*, vol. 89, no. 2, pp. 245–255, 1975.
- [17] J. Vetter, "Chitin content of cultivated mushrooms *Agaricus bisporus*, *Pleurotus ostreatus* and *Lentinula edodes*," *Food Chemistry*, vol. 102, no. 1, pp. 6–9, 2007.
- [18] K.-S. Lin, Y.-J. Mai, S.-R. Li, C.-W. Shu, and C.-H. Wang, "Characterization and hydrogen storage of surface-modified multiwalled carbon nanotubes for fuel cell application," *Journal of Nanomaterials*, vol. 2012, Article ID 939683, 12 pages, 2012.
- [19] S. Kiel, O. Grinberg, N. Perkas, J. Charmet, H. Kepner, and A. Gedanken, "Forming nanoparticles of water-soluble ionic molecules and embedding them into polymer and glass substrates," *Beilstein Journal of Nanotechnology*, vol. 3, no. 1, pp. 267–276, 2012.
- [20] X. Yang, C. Li, W. Wang, B. Yang, S. Zhang, and Y. Qian, "A chemical route from PTFE to amorphous carbon nanospheres in supercritical water," *Chemical Communications*, no. 3, pp. 342–343, 2004.



**Hindawi**

Submit your manuscripts at  
<http://www.hindawi.com>

